Electronic Supplementary Information (ESI)

for

Tracking the active phase and reaction pathway of the OER mediated by an MnMoO$_4$ microrod electro(pre)-catalyst

Anubha Rajput,[†] Ankita Kumari,[†] Hirak Kumar Basak,[†] Dibyajyoti Ghosh,[†§]* and Biswarup Chakraborty[†]*

[†]Department of Chemistry, Indian Institute of Technology Delhi, Hauz Khas, 110016, New Delhi, India

[§]Department of Materials Science and Engineering, Indian Institute of Technology Delhi, Hauz Khas, 110016, New Delhi, India

*E-mail: dibyajyoti@mse.iitd.ac.in and cbiswarup@chemistry.iitd.ac.in

Table of Contents

Characterization and Analysis Methods

1.1. Powder X-ray diffraction (PXRD)

The phase purity and crystallinity of $MnMoO_4$ were characterized by powder X-ray diffraction study on Bruker D8 Advance X-ray diffractometer equipped with Cu Kα (Kα_1 = 1.540598 Å, Kα_2 = 1.544426 Å, Kα ratio 0.5, Kα_{av} = 1.541874Å) X-ray tubes. The diffraction pattern was recorded within the 2θ range of 10° to 80°. The obtained diffractogram was matched with the respective JCPDS (Joint Committee on Powder Diffraction Standards) data file of the reported materials to establish the phase purity.

1.2. Fourier Transform Infrared spectroscopy (FTIR)

FTIR study was done to determine the type of bonding and functional groups present in the material. To do the study, a KBr palette containing the sample was made. To approximately 0.1-0.2 mg of sample few milligrams of KBr powder was added and the mixture was homogenized with mortar pestle. This powder was used to make a palette by applying hydraulic pressure of 3 tonns. The FTIR study was done using the palette with Nicolet, Protege 460 instrument.

1.3. Field Emission Scanning Electron Microscope (FESEM)

FESEM was done to do microstructural analysis of the synthesized nanomaterials. Alongside, Energy dispersive X-ray spectroscopy (EDX) for mapping and elemental analysis was also done. The aforementioned techniques were done for samples before and after electrocatalysis through JSM-IT300HR, JEOL instrument.

1.4. Transmission Electron Microscopy (TEM)

The high resolution transmission electron microscopy (HRTEM) images and selected area electron diffraction (SAED) patterns were recorded using the Thermo-fisher Technie microscope working at accelerate voltage 200 kV. The TEM sample was prepared using 15 μl dilute suspension $MnMoO_4$ in HPLC grade acetone (Merck, India) and by depositing the solution on the 200-mesh carbon coated Cu grids [TED PELLA, INC].

1.5. X-ray Photoelectron Spectroscopy (XPS)

The surface study of the as-synthesized material was done to find out the elemental composition of surface and the valence state of the chemical species present on the material surface with the help of X-ray photoelectron spectroscopy (XPS). The measurement was done using ESCA+, omicron nanotechnology, Oxford Instrument Germany, equipped with aluminium monochromator with aluminium source (Al Kα radiation hv =1486.7eV). The operational voltage and current of the instrument were at 15 kV and 15 mA, respectively.

1.6. Electron Paramagnetic Resonance (EPR)

EPR spectra of the Mn samples were recorded in a Bruker EPR spectrometer (Biospin, EMXmicro A200) at room temperature setup.

1.7. Brunauer–Emmett–Teller (BET) Analysis.

The nitrogen adsorption-desorption and pore size distribution studies were performed using BELSORP-maxII (BELSPRP-series) instrument, acquired from Microtrac BEL Corporation. The instrument was operated by constant volume gas adsorption method coupled with AFSMTM. The nitrogen adsorption-

desorption analysis was conducted out at constant temperature of 77 K. Before analysis, the sample was pre-treated by gas-degassing method to cancel out any interference from adsorbed water or any other gases.

1.8. UV-vis kinetic study.

Kinetic study for the potential-driven and alkaline degradation of $MnMoO_4$ and rate of $[MoO_4]^{2-}$ dissolution into the electrolyte was performed in a dual-beam Agilent Cary 60 UV-Vis spectrophotometer instrument having an 80 Hz Xe flash lamp which can be operated in the wavelength range of 190 to 1100 nm.

1.9. Raman spectroscopy.

Raman spectroscopy of all the material was recorded with HORIBA EVOLUTION, HORIBA Jobinyvon, France, equipped with 532 nm lasers. All the samples were set at 50X and crystalline Si was used for calibration. Raman spectra were recorded with the as-synthesized powder $MnMoO_4$ materials placing them on the Al foil. To detect the reactive oxide phase formed during electrocatalysis with $MnMoO_4$ deposited on nickel foam, the potentiostat was placed adjacent to the Raman spectrometer and Raman spectra were recorded with the $MnMoO_4$/NF electrodes removed from the electrolyte of the three-electrode cell set-up immediately after stirring in KOH, recording cyclic voltammograms, or chronoamperometric study.

1.10. Inductively coupled plasma mass spectrometry (ICP-MS)study.

ICP-MS for the material and the electrolyte after chronoamperometry study was recorded through Agilent ICP-MS 7900.

1.11. density functional theory (DFT) study.

The DFT based calculations used the Vienna ab initio Package (VASP).[1] Here, the exchange-correlation interactions are approximated using the generalized gradient approximation (GGA) formulated by Perdew–Burke–Ernzerhof (PBE).[2, 3] All calculations employ projected augmented wave (PAW), scalar relativistic pseudopotentials, and plane-wave basis sets with a cutoff of 420 eV. The dispersion correction as prescribed by Grimme (DFT-D3) was also used to ensure accurate results.[4] The structures are relaxed until the interatomic Hellmann-Feyman forces become less than 0.01 eV/Å. To investigate the OER activities on δ-MnO_2, a 4×3×1 supercell was created to model the δ-MnO_2 ($2\bar{1}\bar{1}6$) surface, and a vacuum of 40 Å was applied along the non-periodic z-direction. Four bottom layers of the structure have been fixed, while all other layers were allowed to relax within the constant cell parameter of bulk δ -MnO_2. The $7 \times 2 \times 1$ and $10 \times 4 \times 1$ Γ-centered Monkhorst–Pack meshes are used for geometry optimization and self-consistent field (SCF) calculations, respectively. The results are visulaized using VESTA software (open source).

The free energy differences for the OER are calculated using the following approach, proposed by Nørskov and coworkers.[5, 6]

$$\Delta G = \Delta E_{ads} + \Delta E_{ZPE} - T \Delta S - \Delta GpH + \Delta G_U$$

where ΔE_{ads} is the computed reaction energy and is given by following equation:

$$\Delta E_{ads} = E_{(total)} - E_{(clean\ slab)} - E_{(adsorbate)}$$

where $E_{(total)}$, $E_{(clean\ slab)}$, and $E_{(adsorbate)}$ are the total energy of the slab with adsorbate, the energy of the clean surface slab, and the energy of isolated adsorbate in the gas phase, respectively, ΔE_{ZPE} and ΔS are the zero-point energy difference and the entropy difference between the adsorbed state and gas phase. The temperature T is set to 298.15K. G_U includes the external potential. The zero point energy term is given by following equation:[6]

$$E_{zpe} = \sum_i \frac{1}{2} h\nu_i$$

The entropy is given by following equation:[6]

$$S_{vib} = R \sum_i \left\{ \frac{h\nu_i/k_B T}{\exp\left(\frac{h\nu_i}{k_B T}\right) - 1} - \ln\left[1 - \exp\left(-\frac{h\nu_i}{k_B T}\right)\right] \right\}$$

where h is Planck's constant, ν is the vibrational frequency, R is the gas constant, T is the absolute temperature, and k_B is Boltzmann constant.

Experimental Section.

Materials and methods. $MnCl_2 \cdot 4H_2O$, $Na_2MoO_4 \cdot 2H_2O$, $MnSO_4 \cdot H_2O$, $KMnO_4$, and $NaCl$ were purchased from the Central Drug (P) House, India. KOH (99.99% based on trace metals analysis, excludes sodium content; trace metal analysis (< 150.0 ppm), sodium (Na) < 500.0 ppm), ethanol and ethylene glycol were obtained from Merck, India. Nickel foam (NF) of thickness 0.5 mm were obtained from RVL Scientific, India. The chemicals were used without further purification and Milli-Q water was used for all the studies.

Solvothermal synthesis of $MnMoO_4$: For the preparation of $MnMoO_4$, 1 mmol of $MnCl_2 \cdot 4H_2O$ was added into a 1:1 mixture of ethylene glycol and water (10 mL), and it was kept on stirring at room temperature for an hour. To the solution, 1 mmol of $Na_2MoO_4 \cdot 2H_2O$ was added with further stirring for 1 h. The resulting solution was transferred to a 25 ml Teflon liner reactor and was kept inside a stainless-steel autoclave. The whole apparatus was then heated in an oven at 180 °C for 12 h. After 12 h, the autoclave was cooled down to room temperature, and some precipitate was obtained at the bottom. The mixture was centrifuged, and the obtained supernatant was discarded. The precipitate was washed thoroughly with deionized water and once with ethanol and then dried in the oven at 60 °C for 2 h in air. The dried powder material was ground in an agate mortar pestle for further study.[7]

Solvothermal synthesis of δ-MnO_2: In the typical synthesis procedure, 1 mmol of $KMnO_4$ and 1 mmol of $MnSO_4 \cdot H_2O$ were dissolved in 10 mL Milli-Q water with magnetic stirring for 15 minutes. Then, 0.1 M NaCl was added and further stirred for 15 min. The resulting solution was transferred to a 25 mL Teflon-lined stainless-steel autoclave and heated at 60 °C for 1 h. The autoclave was allowed to cool to room temperature after the reaction. Centrifugation was used to separate the precipitates from the supernatant solution, which were then washed with milli-Q water then dried in the air at 60 °C for 2 h in air.[8]

Preparation and deposition of catalyst ink on the electrode surface. Three dimensional and porous network like nickel foam (NF) of thickness ca. 0.5 mm was chosen as electrode substrates for catalyst deposition. The following steps were sequentially employed to prepare a catalyst ink and subsequently to deposit it on NF. First, the NF sheet was cut in several pieces of dimension 1 × 2 cm². It was then

washed ultrasonically in 0.1 M HCl followed by washing twice with milli-Q water and once with acetone. The electrodes were then dried at 50 °C overnight in an oven. Second, to prepare the ink, Nafion was used as a medium to disperse the catalyst in aqueous medium. Nafion was first diluted to 1.0 wt% in ethanol and 50 mg $MnMoO_4$ was added into it. The mixture was homogenized by sonicating the mixture for 10 minutes at room temperature. Third, the prepared ink was drawn in a pipette and was deposited dropwise on a pre-cleaned NF surface. The 1×1 cm^2 surface area was covered with ink after which the electrode was left to dry at room temperature overnight. The same procedure was followed to prepare δ-MnO_2 loaded NF electrodes.

Electrochemical measurement. To study the electrocatalytic activity, a potentiostat (Gamry Interface 1010E) instrument controlled by Echem Analyst™ Software was used for electrochemical measurements and the Origin software was used to further analyze the data. The electrochemical study was done typically in a three-electrode system using 1 M KOH electrolyte (pH 13.6). Among the three electrodes, NF loaded with catalyst was used as a working electrode (WE), A graphite rod (GR) was used as a counter electrode (CE) and a Hg/HgO/1 M KOH electrode (E^o = 0.098 V vs. RHE) was used as a reference electrode (RE).

The CV and LSV were measured to study the electrochemical OER. The electrochemical measurement (CV and LSV) was done with a manual 85% iR compensation (R = resistance of solution including the test electrode), the uncompensated resistance was estimated as the high frequency limit of the real part of impedance. In 1 M KOH, the reference potential with respect to Hg/HgO/1 M KOH was converted to reversible hydrogen electrode (RHE) by using following relation (equation S1):

$$E(RHE) = E\left(\frac{Hg}{HgO}\right) + 0.098V + (0.059 \times pH)V$$

Equation S1

To study the oxygen evolution reaction (OER), the potential range 1.0 V to 1.8 V (*vs*. RHE) was used with a scan rate of 1 mV s^{-1}. The obtained polarographs were used to calculate the overpotential at a fixed current density. Ten cycles of CV were performed prior to LSV in order to activate the catalyst, to get a stable activity and to see the change in catalyst.

Tafel slopes were calculated from the slope of the overpotential (η) versus the logarithm of current density (log *j*) plot and the slope was determined from the kinetically controlled region of the curve. The Tafel slope was calculated according to the Tafel equation:

$$\eta = (b)log(j) + a$$

Equation S2

where η is the overpotential (V), *j* is the current density (mA cm^{-2}), and b is the Tafel slope (mV dec^{-1}).

Out of the deposited amount of catalyst, the fraction of it taking part in the catalytic activity is determined by electrochemical surface area (ECSA). The ECSA was determined from the experimentally determined double layer capacitance (C_{dl}) of the catalyst. C_{dl} was determined by recording cyclic voltammograms of each catalyst in a non-faradic region of 0.8953 V to 0.9953 V (*vs*. RHE) in 1 M KOH at varying scan rates (i.e., 10, 25, 50, 100, 150, and 200 mV s^{-1}). To determine the C_{dl}, the difference between charging and discharging current was measured for each CV cycle at the midway potential and was then plotted against scan rate. This slope represents the C_{dl} at the electrode-electrolyte interface.[9] The ESCA was calculated from the following equation:

$$ESCA = \frac{C_{dl}}{C_s}$$

Equation S3

where C_s is the specific capacitance of the sample or the capacitance of an atomically smooth planar surface of the material per unit area under identical electrolyte conditions. A C_s value of 0.04 mF cm^{-2} was considered for the ECSA calculation.[10]

The chronoamperometric (CA) study was done to understand the stability of the catalyst i.e., its durability without substantial loss in activity. CA was performed in 1 M KOH, for 12 h at a constant potential.

Electrochemical impedance spectroscopy (EIS) was recorded in a frequency region of 100 mHz to 1 MHz, and the obtained data is plotted as Re (Z) vs Im (Z) (Nyquist plot). The obtained semi-circular data in the Nyquist plot was fitted with an equivalent RC circuit model. The charge-transfer resistance (R_{ct}) of the electrode was determined with the help of the semicircle of the Nyquist plot[11] where the impedance at high frequency region denotes the solution resistance (R_s) and the difference between impedance at higher and lower frequency represents the R_{ct}.

The TOF indicates the moles of oxygen evolved from per moles of total metal content per second (s^{-1}). For electrocatalysts, TOF can be calculated from the following equation.

$$TOF\ (s^{-1}) = \frac{j \times A}{Z \times F \times n}$$

Equation S4

where, j = OER current density, A = geometrical electrode surface area, F = 96485.33289 C mol^{-1}, Z = 4 electron transfer in overall reaction, and n = mole number of transition metal.

Faradaic efficiency (F.E.) is the capability of the catalyst to allow the passage of electrons (charge) through it to facilitate the electrochemical reaction. The F.E. of $MnMoO_4$ for OER was tested in 1 M KOH in a two electrode cell having graphite rod as a cathode while $MnMoO_4$/NF as the anode. The oxygen gas evolved at the anode and hydrogen gas evolved at the cathode was quantified by the change in volume of the electrolyte.

$$FE\ (O_2, \%) = \frac{n \times F \times E}{i \times t} \times 100\%$$

Equation S5

where n is the number of electrons involved, F is the Faraday constant (96485.33289 C/mol), E is the moles of oxygen generated, i indicates the current density, and t is the time (s) period for the electrolysis.

Table S1. Electrocatalytic OER/HER/Overall water splitting performance of some reported Mn-based catalysts.

Catalyst	substrate	Electrolyte	η_{HER} (mV)@ 10 mA	η_{OER} (mV)@ 10 mA	Overall water splitting (V)@10 mA	Active species	Reference
Hydrogenated $MnMoO_4$	NF (in-situ)	1.0M KOH	179[a]	-	-	-	[12]
$MnMoO_4$	NF (in-situ)	0.5M H$_2$SO$_4$	89	-	-	-	[13]
		1.0M KOH	105	-	-	-	
		1.0M PBS (pH=7)	161	-	-	-	

Catalyst	Substrate	Electrolyte					Ref
PANI–MnMoO$_4$	NF	1.0M KOH	155	410 mV[b]	1.65	-	14
MnMoO$_4$	Ni electrode	1.0 M KOH	-	400	-	-	15
NiMn$_2$O$_4$	NF	1.0 M KOH	248	250	1.69	-	16
MnGa$_4$	NF	1.0 M KOH	-	293	-	δ-MnO$_2$, β-MnOOH, α-Mn$_3$O$_4$	17
Mn$_3$N$_2$	NF	1.0 M KOH	-	270	-	MnO$_x$	18
LiMnBPO	FTO	1.0 M KOH	-	322	-	δ-MnO$_2$	19
MnS	NF	1.0 M KOH	-	294	-	δ-MnO$_2$	20
MnO$_x$/NF	NF	1.0 M KOH	-	280[c]	-	Mn^{III} sites	21
MnO$_2$	GC-RDE	1.0 M KOH	271	449	-	-	22
MnNi-hydroxide	NF		231	327		-	23
IrO$_x$/ε-MnO$_2$	carbon fiber paper	0.5 M H$_2$SO$_4$	-	225	1.65 V	Ir	24
IrO$_x$/α-MnO$_2$			-	242	-		
IrO$_x$/δ-MnO$_2$			-	286			
β-MnO$_2$	FTO	1.0 M NaOH	-	500	-	-	25
Amorphous MnO$_2$	pyrolytic graphite carbon	0.1 M KOH	-	490	-	-	26
α-MnO$_2$			-	590	-	-	
β-MnO$_2$			-	600	-	-	
δ-MnO$_2$			-	740	-	-	
α-Mn$_2$O$_3$	F@SnO$_2$/ glass	1 M KOH	-	570[d]	-	-	27
MnO$_x$			-	570[d]	-	-	
Mn$_3$O$_4$			-	570	-	-	
α-MnO$_2$	NF	1 M KOH	-	450[e]	-	oxygen vacancies and Mn ion defects	28
δ-MnO$_2$			-	530[e]	-		
δ-MnO$_2$	NF (in situ)	1 M KOH	196	320	-	Unsaturated Mn^{3+} sites	29
β-MnO$_2$-VO$_2$(B)/2D-rGO	GC	3 M KOH	178	273	1.62 (on NF)	-	30
IrO$_2$@α-MnO$_2$	Ti plate	0.1 M HClO$_4$	-	275	-	IrO$_2$	31
K$_x$Fe[Co$_{0.16}$Mn$_{0.84}$O$_2$]	FTO	1 M KOH	-	375	-	FeO$_x$	32
Mn$_3$O$_4$/CoSe$_2$	GC	O$_2$-saturated 0.1 M KOH	-	450	-	Co^{IV}	33
MnO NPs	FTO	0.5 M phosphate buffer	-	530[f]	-	Mn^{III}	34
MoS$_2$/MnMoO$_4$@Ti	Ti foil	0.5 M H$_2$SO$_4$	153	-	-	Mo edge	35
Mo doped Mn$_2$O$_3$	FTO	1.0 M H$_2$SO$_4$		570			36
MnSe@MWCNT	CC	N$_2$-saturated 1 M KOH	-	290	-	(oxy)selenide	37
Mn-N doped graphene	Graphite plate	1 M KOH	-	337	-	MnN$_4$-G	38

[a]@5mA, [b]@30mA, [c]@100mA, [d]@20mA, [e]@50mA, [f]@5 mA, Nickel foam (NF), Fluorinated tin oxide (FTO), Glassy carbon-rotating disk electrode (GC-RDE), Glassy carbon (GC), Carbon cloth (CC).
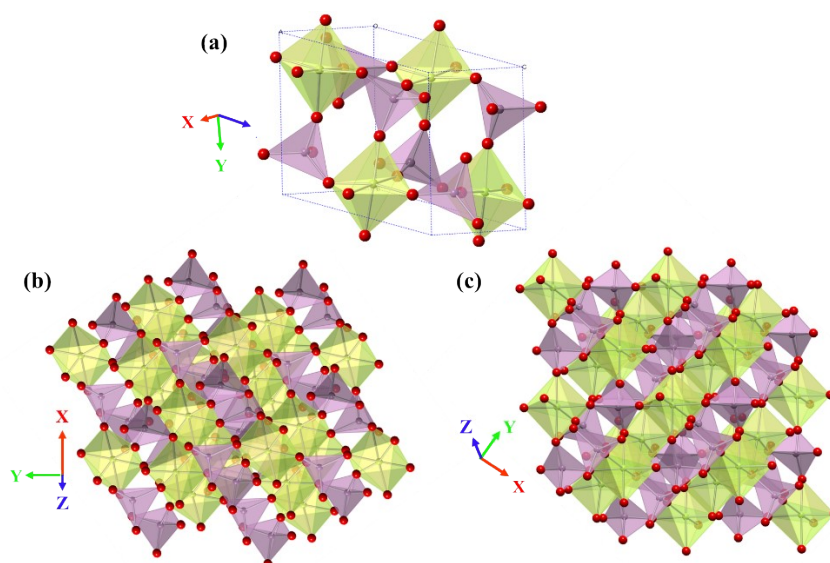
Figure S1. (a) A single unit cell of MnMoO$_4$. (b-c) The extended 3-D polyhedral presentation of the interconnected units of [MnO$_6$] and [MoO$_4$] in different spatial orientations of M^{II}Mo^{VI}O$_4$. Purple polyhedron = Mo; green polyhedron = Mn.
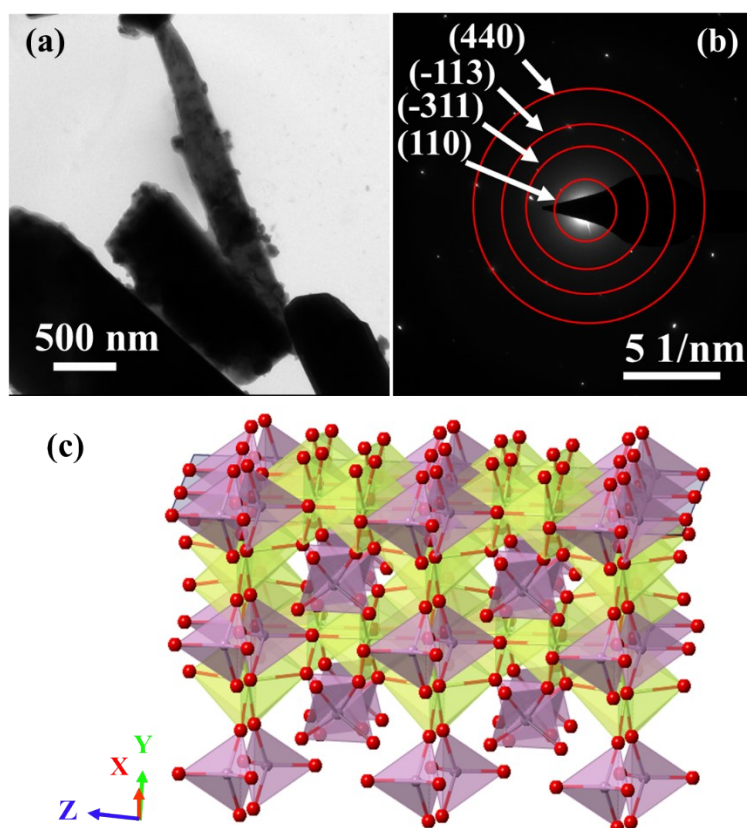

Figure S2. (a) HR-TEM images of the as-synthesized MnMoO$_4$. (b) SAED pattern of as-synthesized MnMoO$_4$ showing the diffraction rings corresponding to the diffractions observed in the PXRD pattern.

(c) The polyhedral presentation of the (220) surface of $MnMoO_4$. (The alternative rows of $[MnO_6]$ and $[MoO_4]$ polyhedra presented at the top consisted of (220) surface).
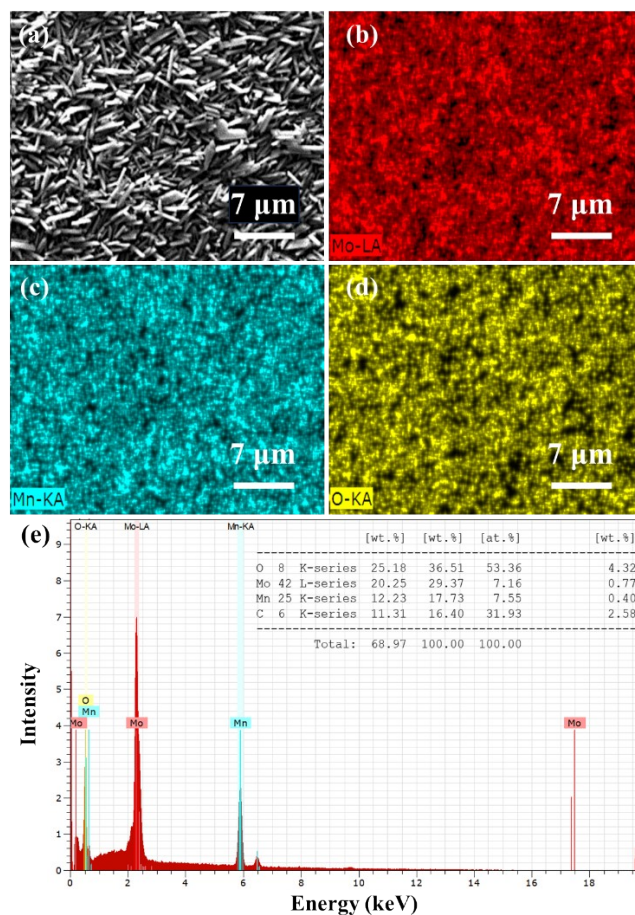
Figure S3. (a-d) SEM-EDX elemental mapping of $MnMoO_4$ showing a homogeneous distribution of Mo, Mn, and O. (e) EDX spectrum of $MnMoO_4$ with the atomic ratio of elements in the inset.

Table S2. A data file of the ICP-MS study of the as-synthesized solid sample and electrolyte at a different time intervals during OER-CA of $MnMoO_4$/NF.

Data File	Vol. (mL)	55 Mn [He] Conc. (ppb)	55 Mn [He] Conc. (µg/g)	95 Mo [He] Conc. (ppb)	95 Mo [He] Conc. (µg/g)	% Mo
$MnMoO_4$ (digested)	-	14775.2	-	15013.9	-	-
$MnMoO_4$ (electrolyte, 2h stir)	40	-	-	3266.1	-	26
$MnMoO_4$ (electrolyte, 2h CA)	40	-	-	4102.0	-	33
$MnMoO_4$ (electrolyte, 12h CA)	40	22.75	-	9067.7	-	83
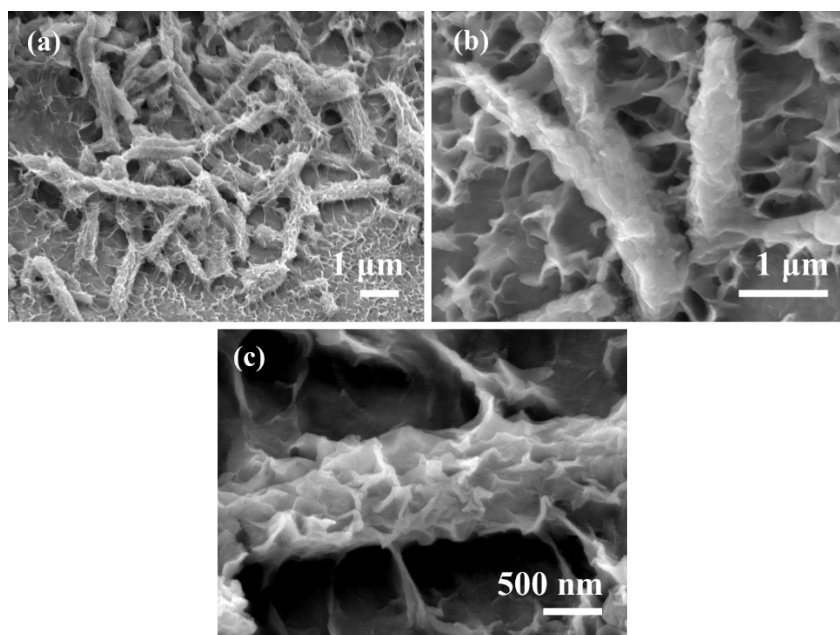
Figure S4. (a-c) FESEM images of the MnMoO$_4$/NF after 2 h OER-CA at different magnifications.

| Element	Wt%	Wt% Sigma	Atomic %
O	35.58	0.50	67.11
Mn	53.80	0.62	29.55
Mo	10.62	0.53	3.34
Total:	100.00		100.00
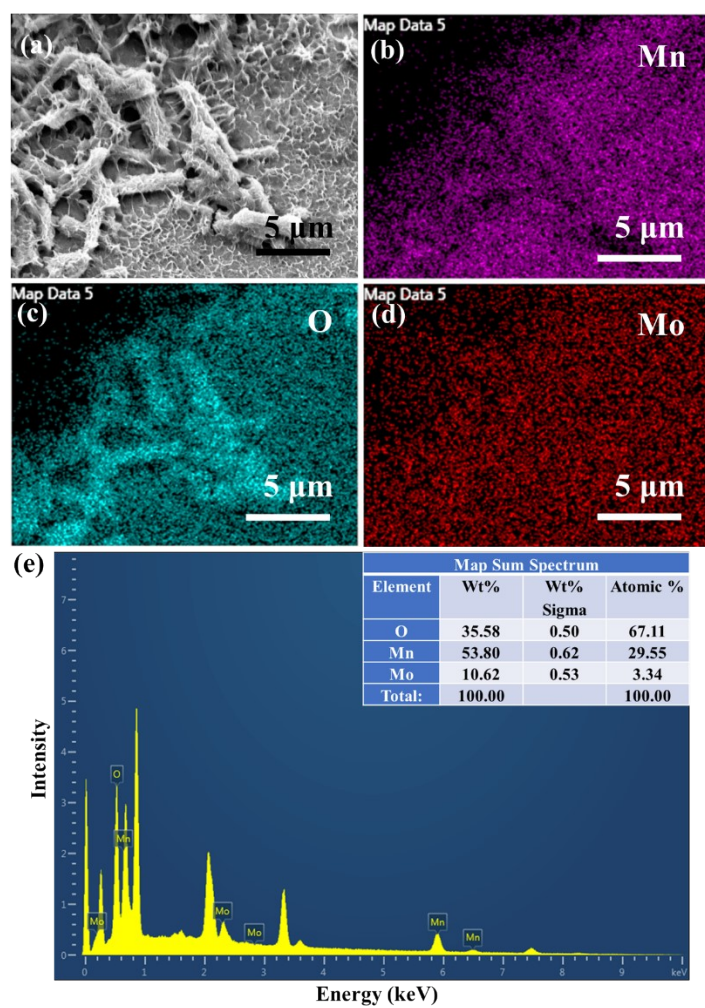
Figure S5. (a-d) SEM-EDX elemental mapping of MnMoO$_4$/NF after 2 h OER-CA. (e) EDX spectrum and the ratio of elements present on the surface showing the decrement in the concentration of Mo.
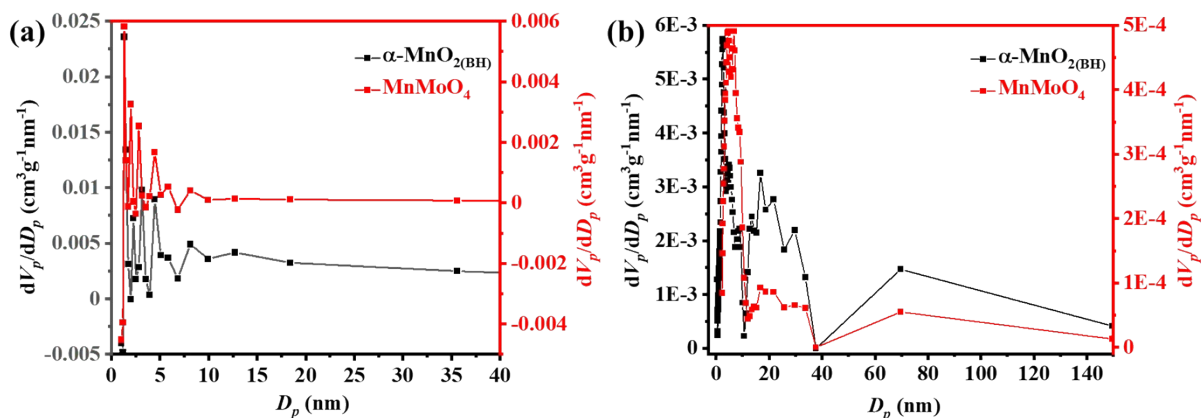
Figure S6. Pore size distribution curves of as synthesized MnMoO$_4$ and MnMoO$_4$ after 2 h OER-CA (α-MnO$_{2(BH)}$) determined by (a) the BJH method and (b) the NLDFT model.
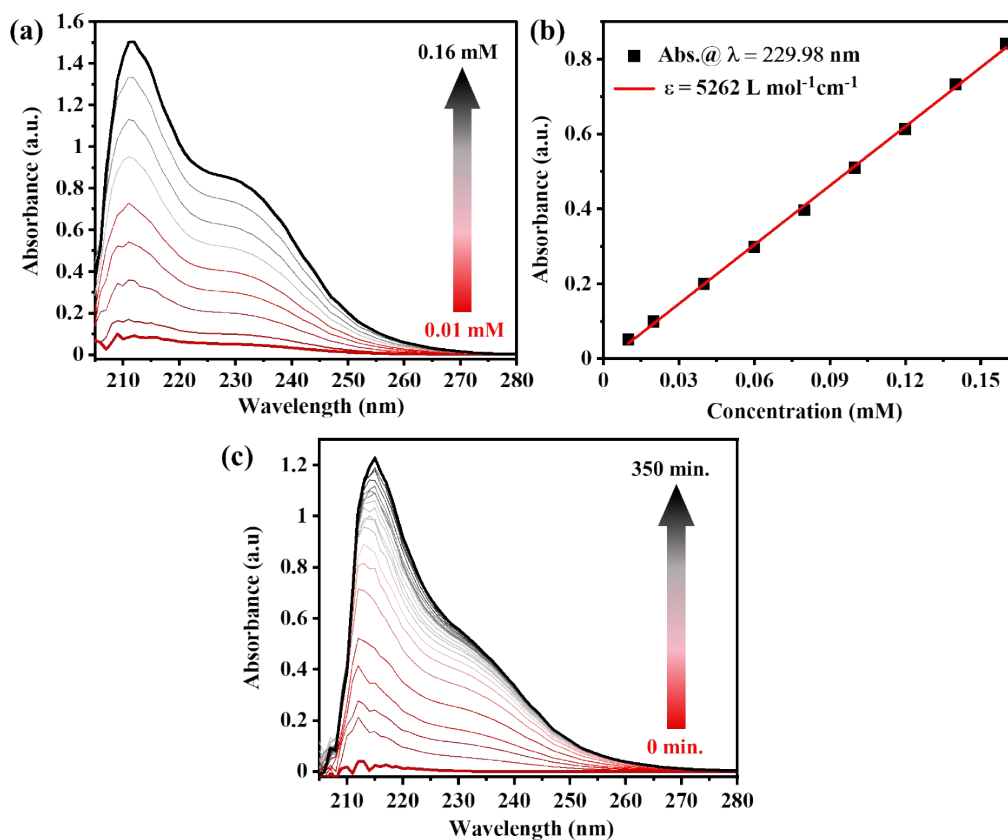
Figure S7. (a) The optical spectra (UV-Vis) of Na$_2$MoO$_4$ (MoO$_4^{2-}$) solution in various concentrations. (b) The calibration curve made form the linear fitting of absorbance vs. concentration of the MoO$_4^{2-}$ during stirring in alkaline conditions. (c) UV-Vis spectra of the electrolyte during the base hydrolysis MnMoO$_4$ catalyst deposited on NF surface. The change in optical spectra with time (red: 0 min and black: 350 mins) which represent the increasing [MoO$_4$]$^{2-}$ as the charge transfer band at 214 nm increased.
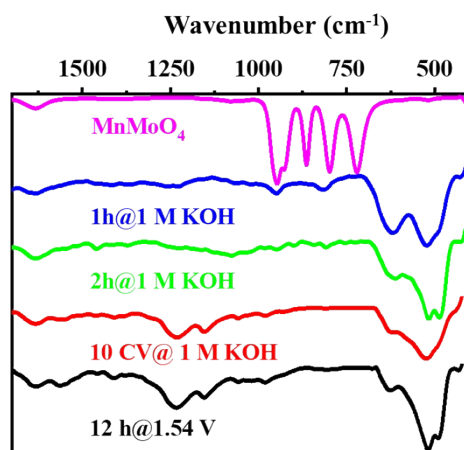
Figure S8. FTIR spectra recorded with the as-synthesized MnMoO$_4$ sample and the catalyst isolated from MnMoO$_4$/NF after different electrochemical studies.
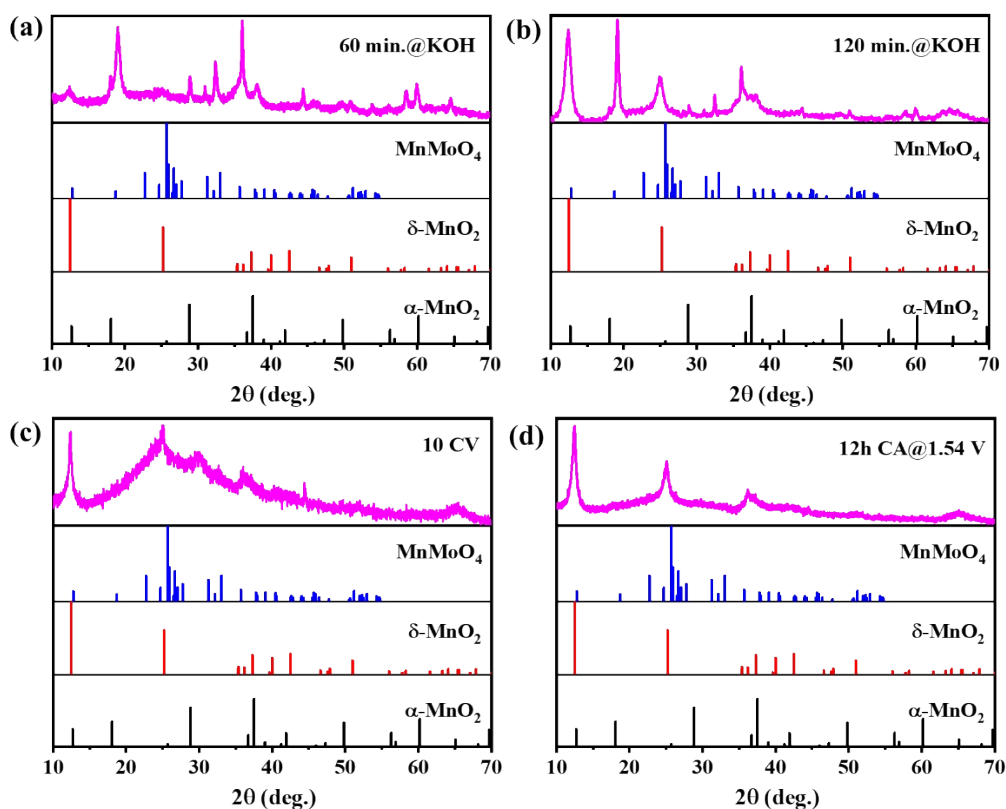
Figure S9. PXRD diffractograms of isolated catalyst from MnMoO$_4$/NF after (a) 60 minutes stirring in 1M KOH, (b) 120 minutes stirring in 1M KOH, (c) 10 CV cycles, and (d) 12 h OER-CA and their comparison with the powder diffraction data of MnMoO$_4$ (JCPDS No. 72-0285),[8] α-MnO$_2$ (JCPDS No. 44-0141),[39] and δ-MnO$_2$ (JCPDS No. 52-0556).[26]
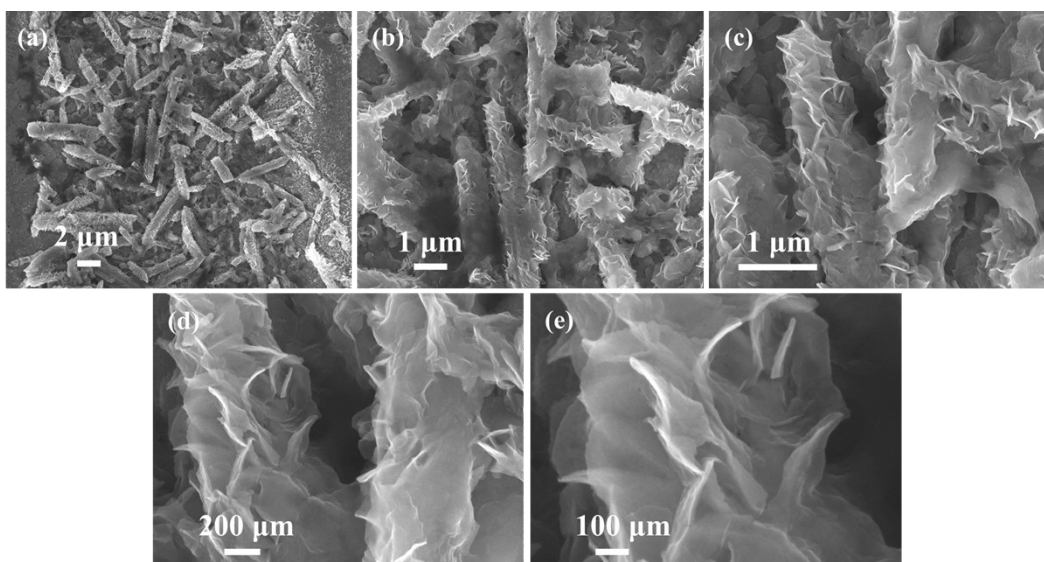
Figure S10. (a-e) FESEM images of the MnMoO$_4$/NF after 12 h OER-CA at different magnifications.
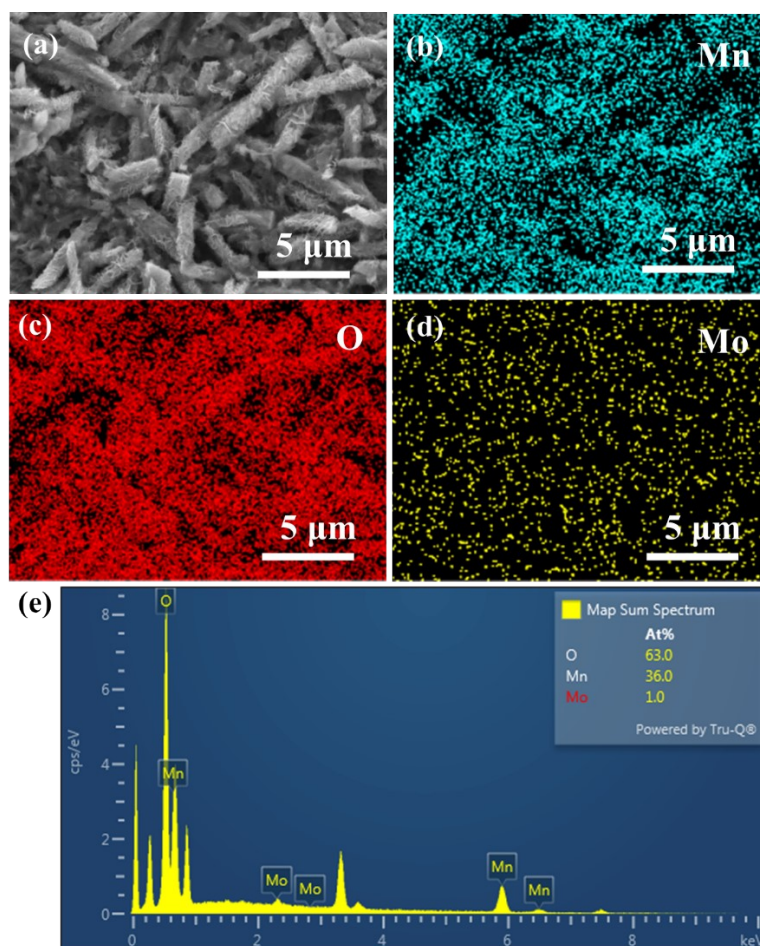
Figure S11. (a-d) SEM-EDX elemental mapping of MnMoO$_4$/NF after 12 h OER-CA. (e) EDX spectrum and the ratio of elements present on the surface showing the drastic loss in the concentration of Molybdenum.
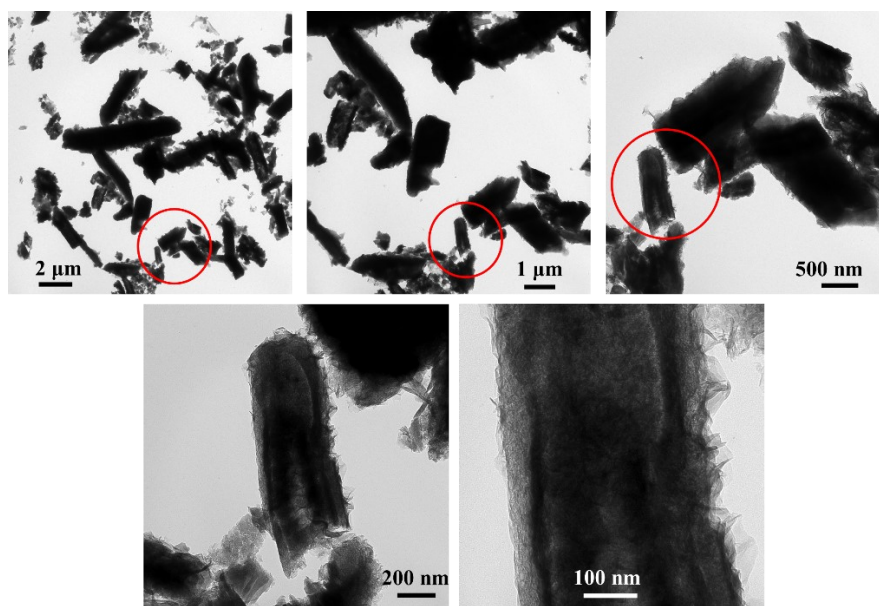
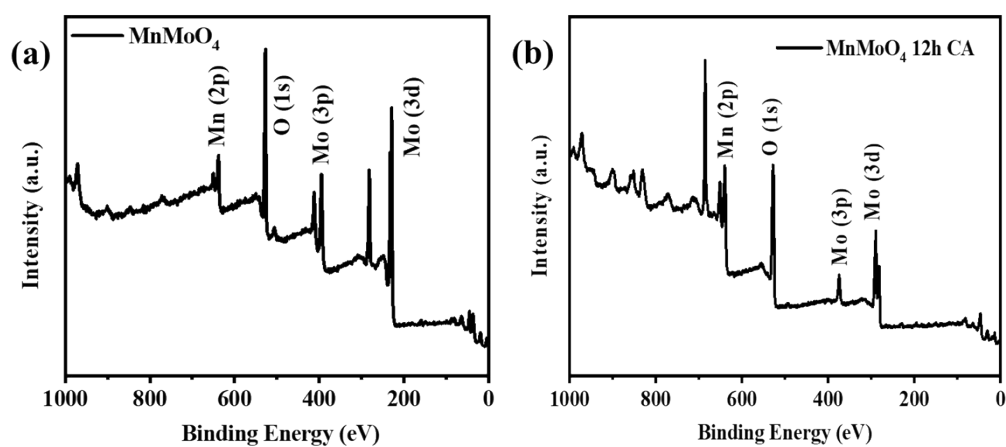**Figure S12.** HRTEM study of the sample isolated from MnMoO$_4$/NF after 12 h OER-CA.

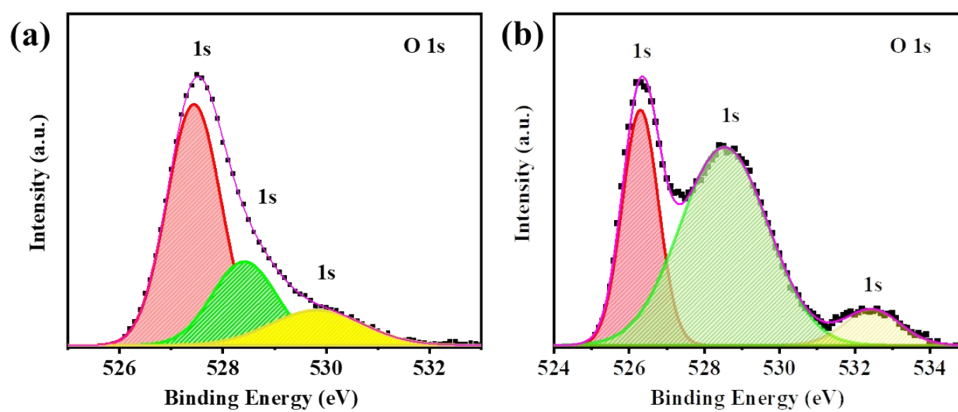**Figure S13.** The XPS elemental survey for (a) MnMoO$_4$ and (b) MnMoO$_4$ after 12 h OER-CA.

Figure S14. Core-level O 1s XPS scans (with deconvolution) of (a) MnMoO$_4$ and (b) MnMoO$_4$ after 12h OER-CA.
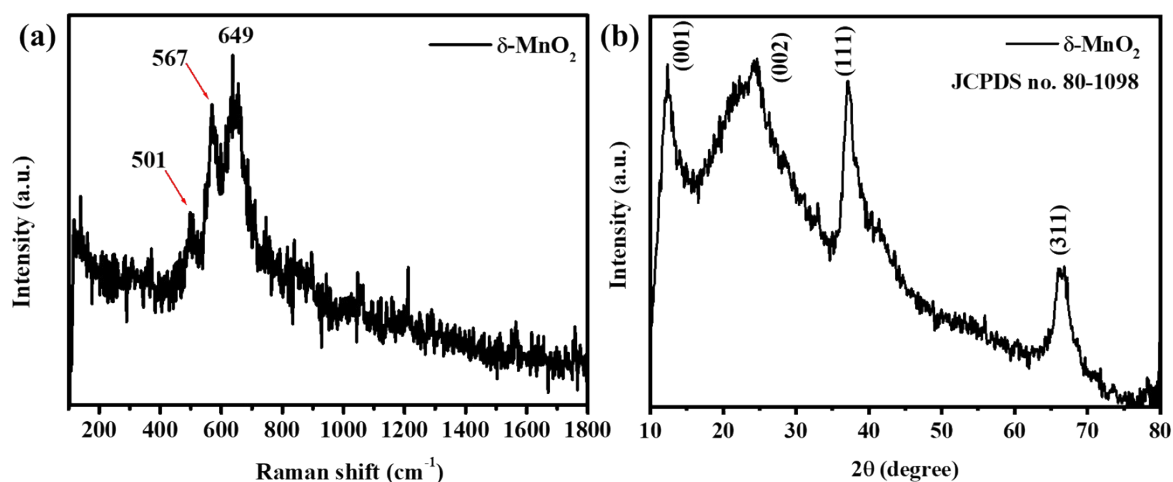
Figure S15. (a) The Raman spectrum and (b) the PXR diffractogram of the ex-situ prepared δ-MnO$_2$.
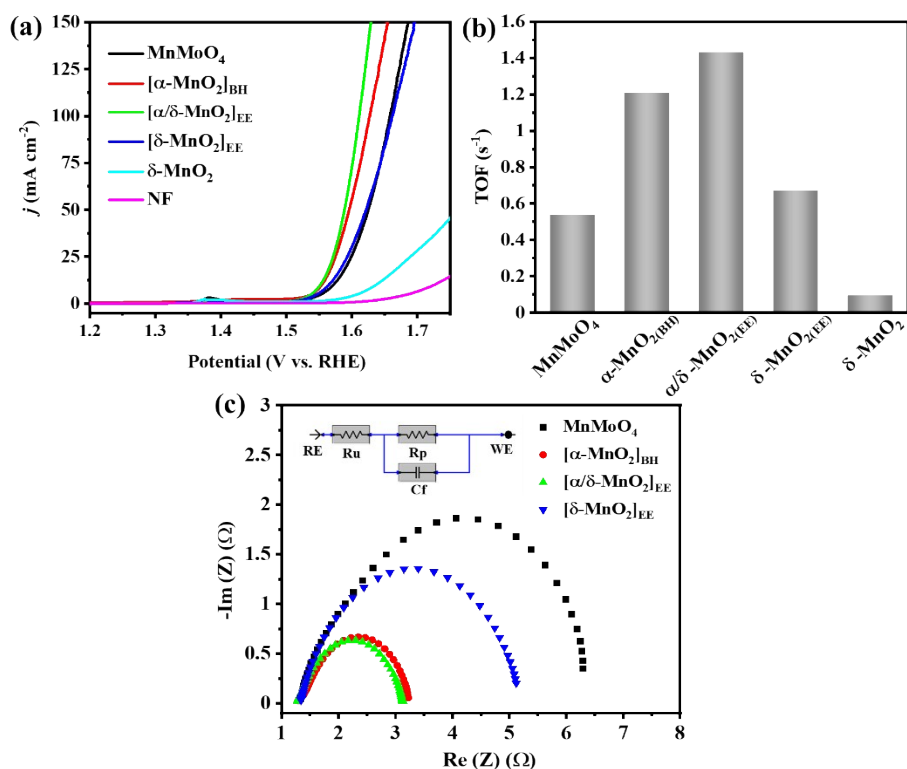

Figure S16. (a) LSV study with MnMoO$_4$, in-situ evolved MnO$_2$, independently prepared MnO$_2$ and nickel foam (NF). (b) The bar chart showing the comparative TOF of MnMoO$_4$, in-situ evolved MnO$_2$, independently prepared MnO$_2$. (c) Corresponding Nyquist plots obtained from electrochemical impedance spectroscopy (EIS). The inset shows the equivalent circuit fitting (R$_u$ = R$_s$ = solvent resistance; R$_p$ = R$_{ct}$ = charge transfer resistance; C$_f$ = C$_{dl}$ = double layer capacitance).
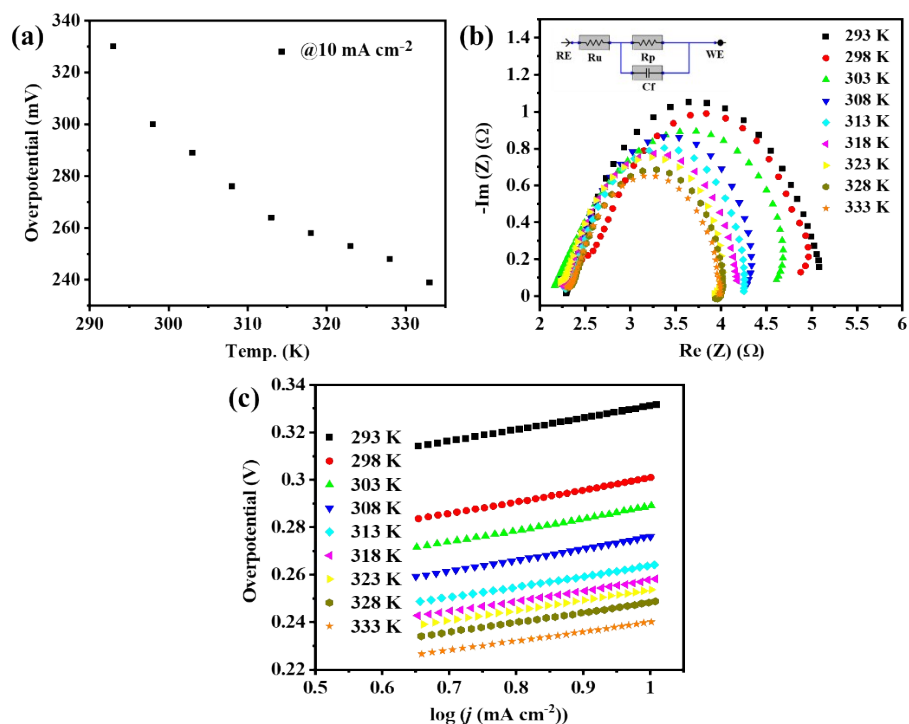
Figure S17. (a) Variation of the overpotential with the cell temperature at a fixed current of 10 mA cm^{-2} for α/δ-MnO$_{2(EE)}$ (b) The Nyquist plots obtained from the EIS study at different temperatures from 293 K to 333 K. The inset shows the equivalent circuit fitting. (c) The corresponding variation of Tafel slope with temperature.

Table S3: The variation of Tafel slope, overpotential, and onset potential with temperature.

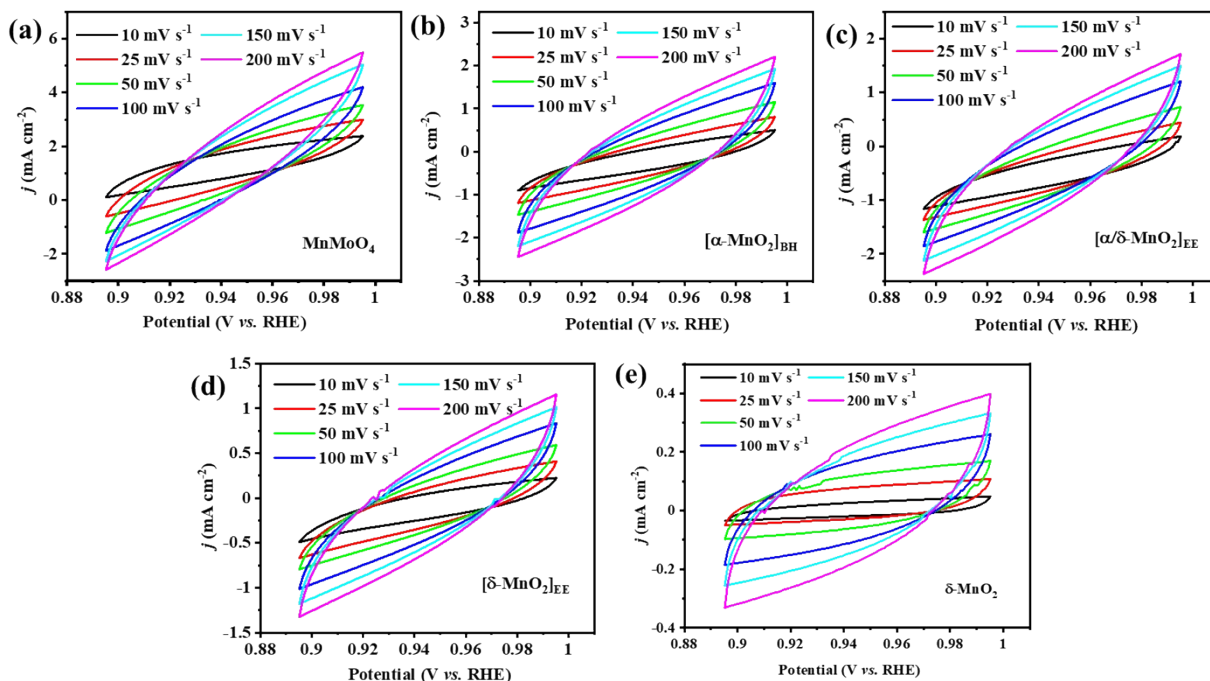| Temperature (K)	Tafel slope (mV dec^{-1})	Overpotential (mV)	Onset Potential (mV)
293	49.4	330	1.499
298	49.9	300	1.477
303	49.7	289	1.463
308	47.9	276	1.453
313	44	264	1.446
318	43.4	258	1.442
323	42.8	253	1.439
328	41.3	248	1.435
333	38.9	239	1.429

Figure S18. ECSA analysis from the CV scans in a non-Faradaic potential range of MnMoO$_4$/NF and the MnO$_x$ materials derived from it at different activations and independently prepared reference δ-MnO$_2$ in 1 M KOH at scan rate of 10 mV s^{-1}, 25 mV s^{-1}, 50 mV s^{-1}, 100 mV s^{-1} and 200 mV s^{-1}.
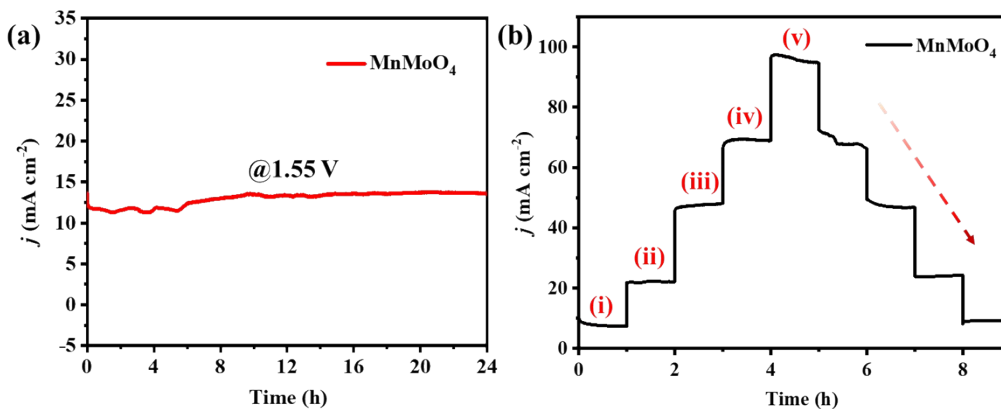

Figure S19. (a) Chronoamperometric study of α/δ-MnO$_{2(EE)}$/NF for 24 hours to establish the durability of the catalysts. (b) Staircase-like plot showing the stability of the catalyst over a wide range of potentials. The stepwise stability at approximate current densities of 10, 25, 50, 75, and 100 mA cm^{-2} have been tested at 1.54 V, 1.63 V, 1.71 V, 1.76 V and 1.83 V (vs RHE), respectively. The steps have been repeated, lowering the current from 100 to 10 mA cm^{-2} at the same respective potentials.
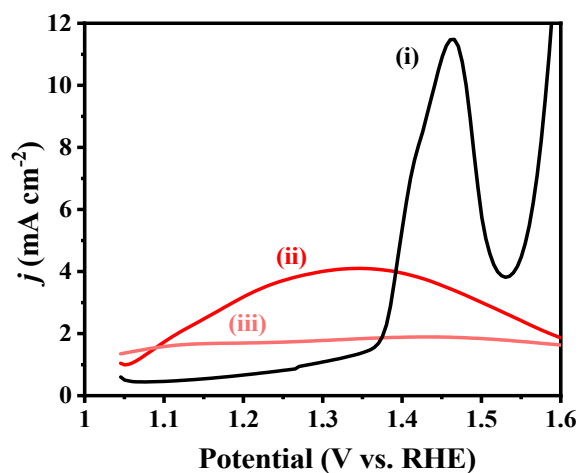
Figure S20. Differential pulse voltammetry of (i) bare NF (ii) MnMoO$_4$/CC without activation and (iii) after potential driven activation showing the rapid loss of redox feature.
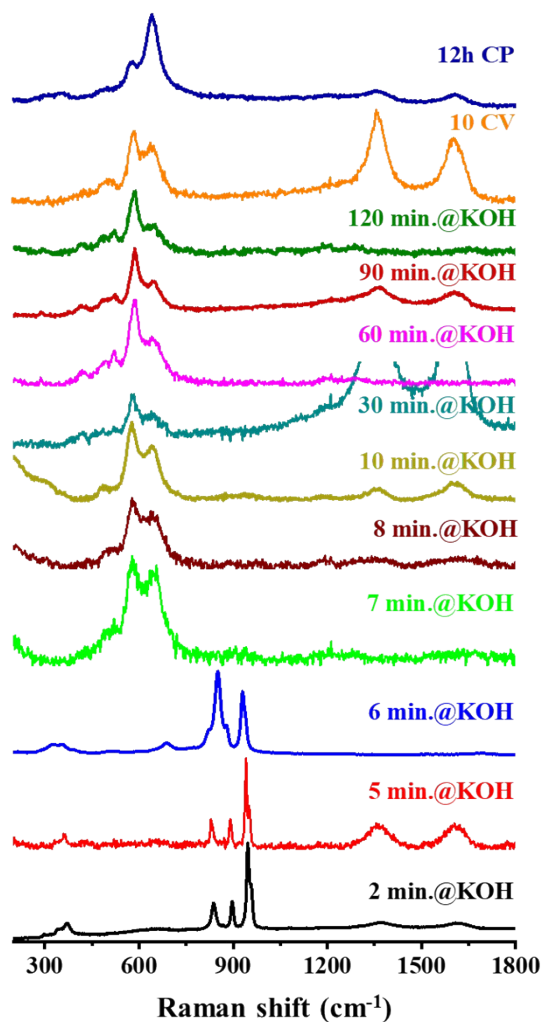

Figure S21. Time-resolved quasi-in situ Raman spectra of MnMoO$_4$/CC in alkaline electrolyte at different stages of activation demonstrating the catalyst transformation independent of electrode support material. (The broad bands within 1250-1750 cm^{-1} corresponds to graphitic layer of the carbon cloth)
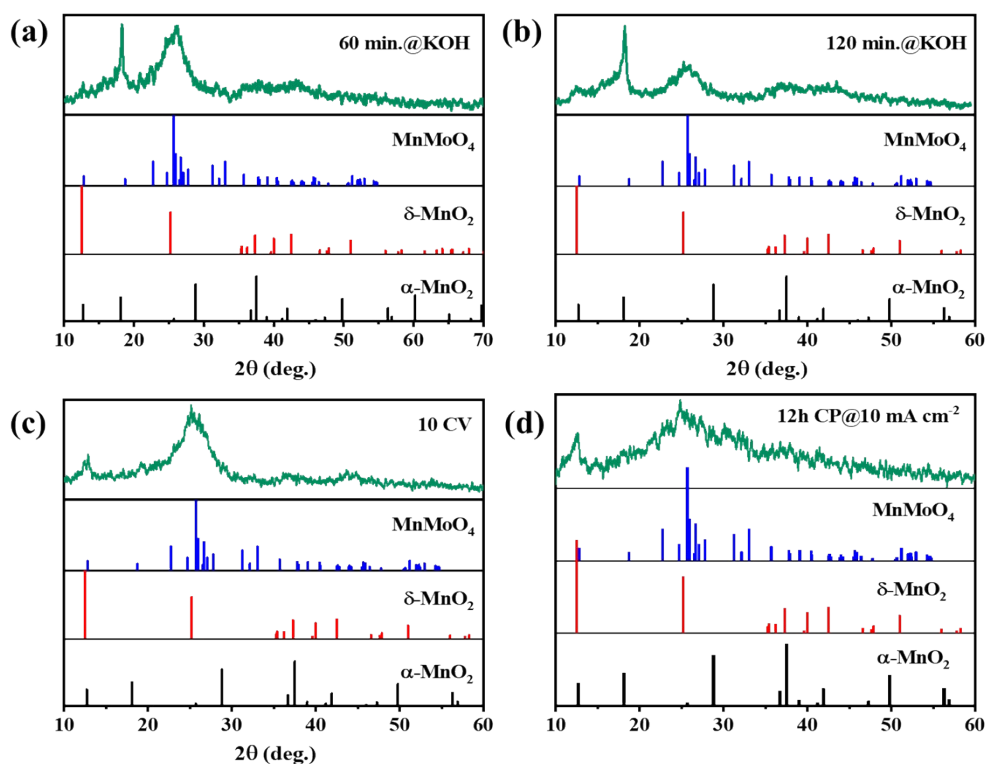
Figure S22. PXRD diffractograms of isolated catalyst from MnMoO$_4$/CC after (a) 60 minutes stirring in 1M KOH, (b) 120 minutes stirring in 1M KOH, (c) 10 CV cycles, and (d) 12 h OER-CP and their comparison with the standard powder diffraction data of MnMoO$_4$, α-MnO$_2$, and δ-MnO$_2$.

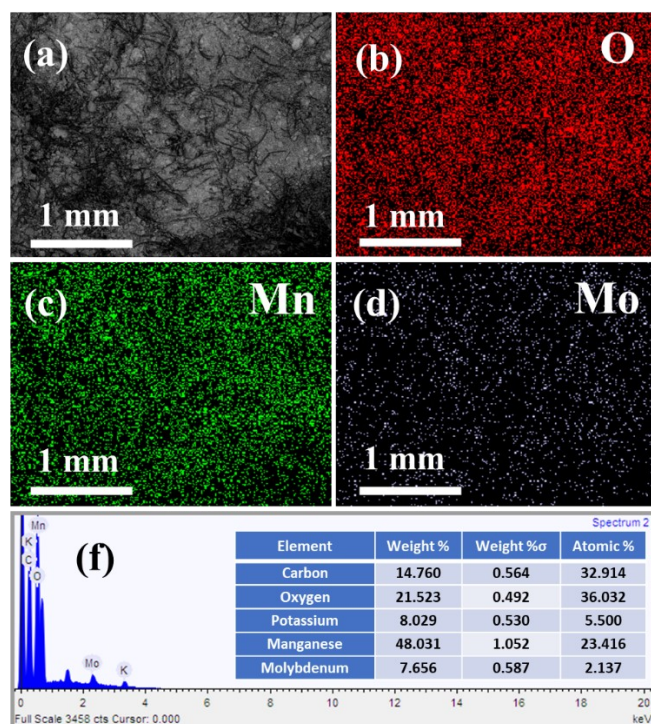| Element	Weight %	Weight %σ	Atomic %
Carbon	14.760	0.564	32.914
Oxygen	21.523	0.492	36.032
Potassium	8.029	0.530	5.500
Manganese	48.031	1.052	23.416
Molybdenum	7.656	0.587	2.137

Figure S23. (a-d) SEM-EDX elemental mapping of MnMoO$_4$/CC after 10 CV cycles. (e) EDX spectrum and the ratio of elements present on the surface.
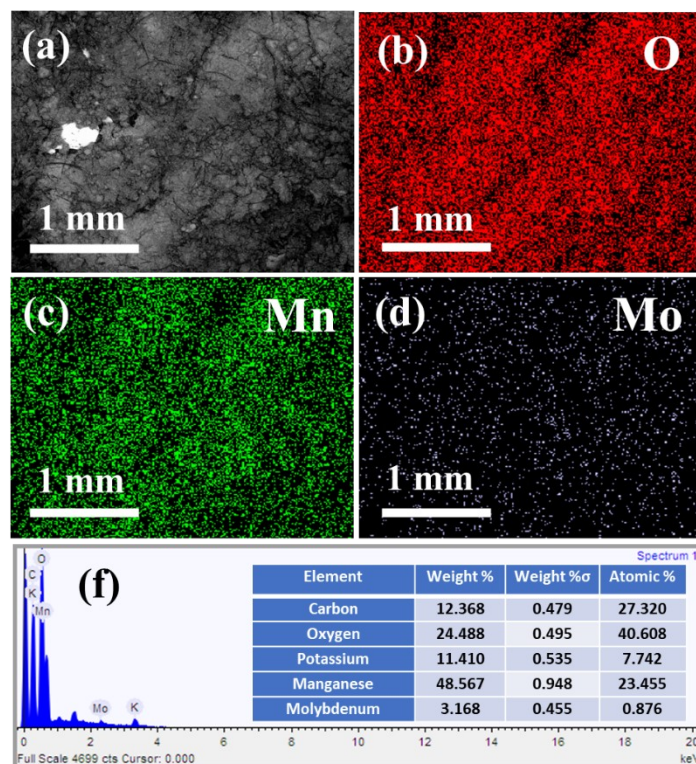
Figure S24. (a-d) SEM-EDX elemental mapping of MnMoO$_4$/CC after 12 h OER-CP. (e) EDX spectrum and the ratio of elements present on the surface showing the loss of molybdenum from the catalyst similar to that on NF.
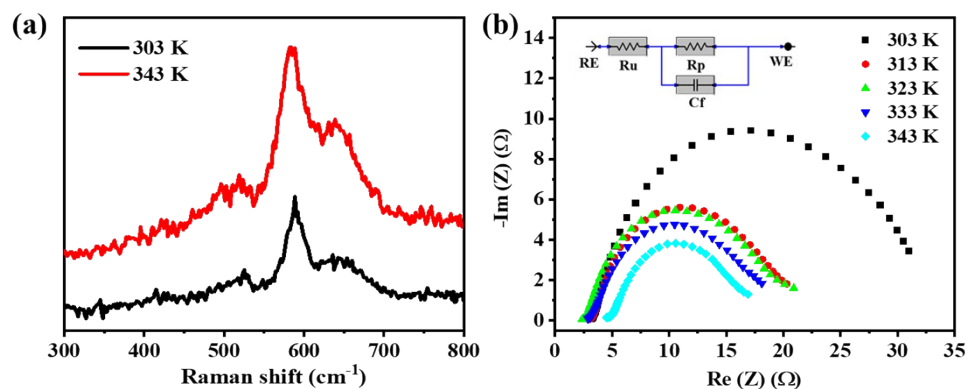
Element	Weight %	Weight %σ	Atomic %
Carbon	12.368	0.479	27.320
Oxygen	24.488	0.495	40.608
Potassium	11.410	0.535	7.742
Manganese	48.567	0.948	23.455
Molybdenum	3.168	0.455	0.876

Figure S25. (a) Raman spectra of α/δ-MnO$_{2(EE)}$/CC before and after the temperature dependent study. (b) The Nyquist plots from the EIS study of α/δ-MnO$_{2(EE)}$/CC at different temperatures. The inset shows the equivalent circuit fitting.
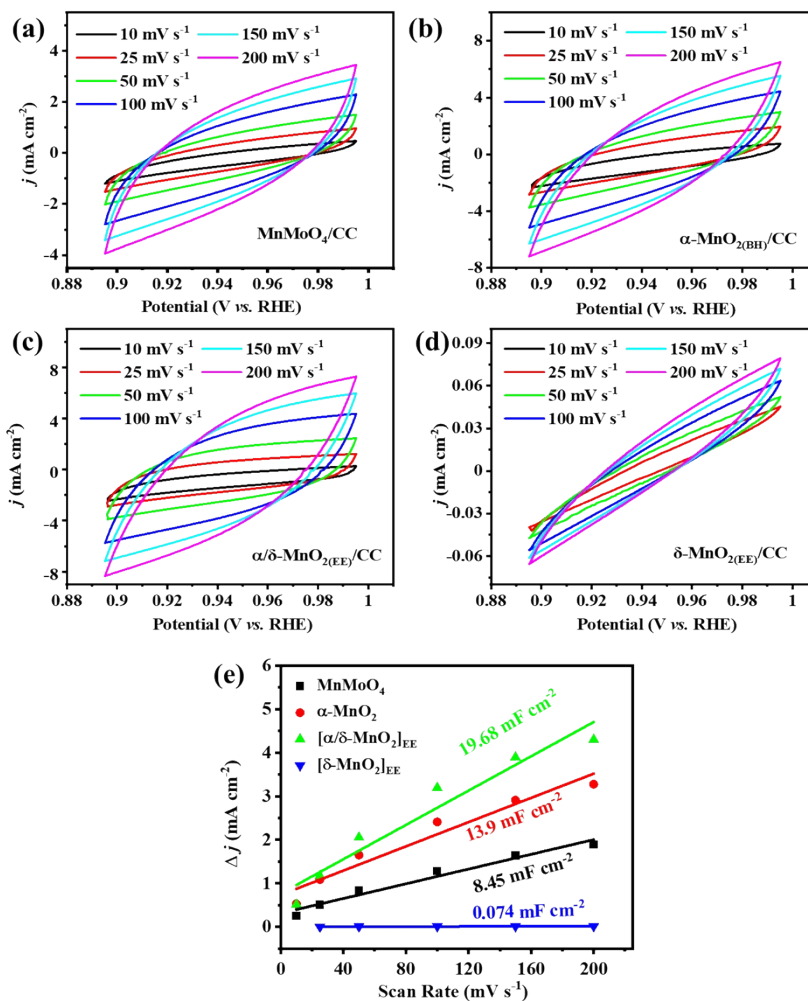
Figure S26. ECSA analysis from the CV scans in a non-Faradaic potential range for MnMoO$_4$/CC and its different activations in 1 M KOH at scan rate of 10 mV s^{-1}, 25 mV s^{-1}, 50 mV s^{-1}, 100 mV s^{-1} and 200 mV s^{-1}. (e) C$_{dl}$ values of MnMoO$_4$/CC and the MnO$_x$ materials derived from it at different activations.
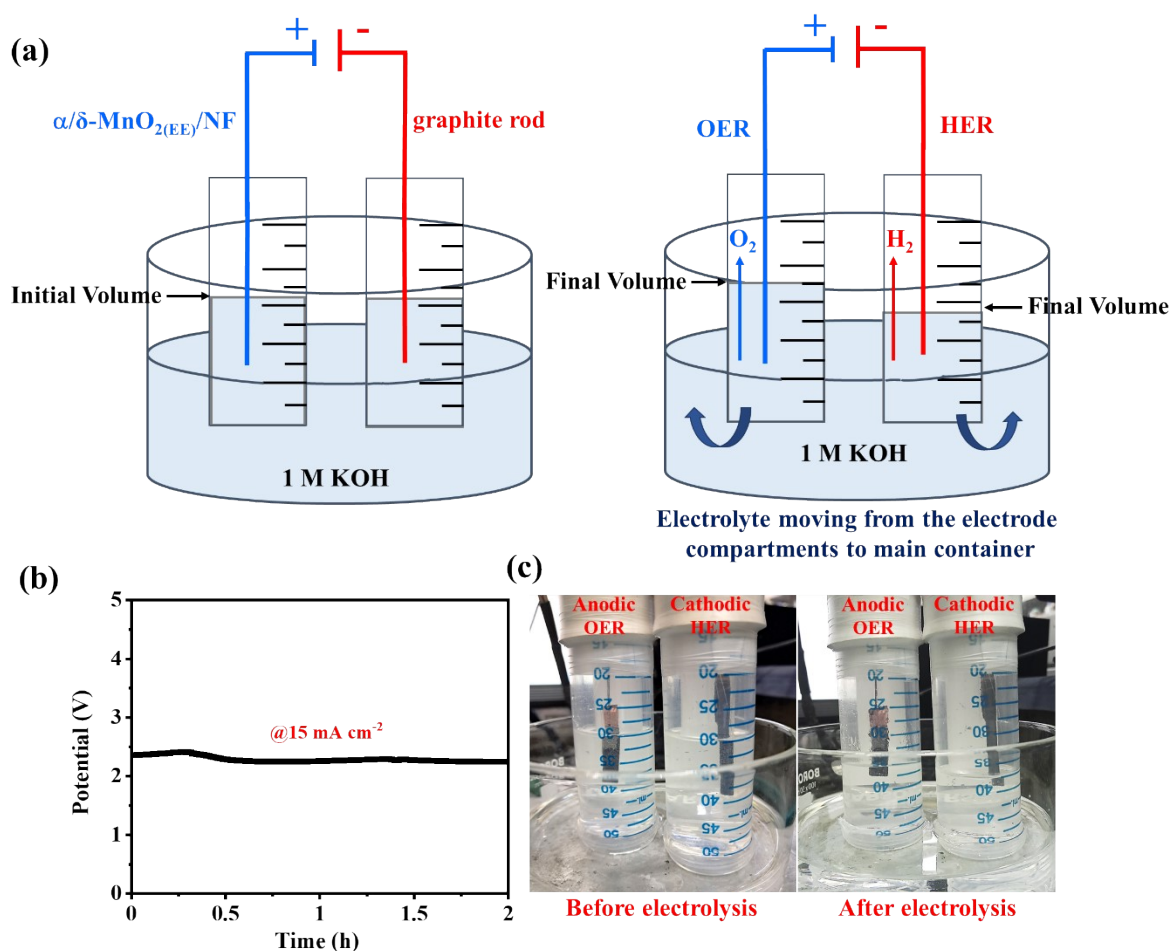
Figure S27. (a) Schematic representation of the assembling and fabrication of a lab-made apparatus for examining the evolved O_2 gas during electrolysis. (b) Chronopotentiometry (CP) carried out for 7200 s in 1 M KOH at a constant current. (c) The change in the volume of KOH after electrolysis showing the evolution of gases in their respective chambers.

References.

1. G. Kresse and J. Furthmüller, *Phys Rev B Condens Matter* 1996, **54 16**, 11169-11186.
2. G. Kresse and D. P. Joubert, *Phys. Rev. B* 1999, **59**, 1758-1775.
3. J. P. Perdew, A. Ruzsinszky, G. I. Csonka, O. A. Vydrov, G. E. Scuseria, L. A. Constantin, X. Zhou and K. Burke, *Phys. Rev. Lett.* , 2008, **100**, 136406.
4. S. Grimme, J. Antony, S. Ehrlich and H. Krieg, *J Chem Phys.*, 2010, **132 15**, 154104.
5. J. K. Nørskov, J. Rossmeisl, A. Logadottir, L. Lindqvist, J. R. Kitchin, T. Bligaard and H. Jónsson, *J. Phys. Chem. B*, 2004, **108**, 17886-17892.
6. J. G. Howalt, T. Bligaard, J. Rossmeisl and T. Vegge, *Phys. Chem. Chem. Phys.*, 2013, **15**, 7785-7795.
7. B. Saravanakumar, S. Ramachandran, G. Ravi, V. Ganesh and A. Sakunthala, *Appl. Phys. A*, 2018, **125**, 6-16.
8. Y. Sun, C. Xu, B. Li, J. Xu, Y. He, H. Du and F. Kang, *Int. J. Electrochem. Sci.*, 2014, **9**, 6387-6401.
9. Q. Kang, L. Vernisse, R. C. Remsing, A. C. Thenuwara, S. L. Shumlas, I. G. McKendry, M. L. Klein, E. Borguet, M. J. Zdilla and D. R. Strongin, *J. Am. Chem. Soc.*, 2017, **139**, 1863-1870.
10. C. C. L. McCrory, S. Jung, J. C. Peters and T. F. Jaramillo, *J. Am. Chem. Soc.*, 2013, **135**, 16977-16987.
11. R. Beltrán-Suito, P. W. Menezes and M. Driess, *J. Mater. Chem. A*, 2019, **7**, 15749-15756.

12. X. Yan, L. Tian, J. Murowchick and X. Chen, *J. Mater. Chem. A*, 2016, **4**, 3683-3688.
13. L. Wen, Y. Sun, T. Zhang, Y. Bai, X. Li, X. Lyu, W. Cai and Y. Li, *Nanotechnology*, 2018, **29**, 335403.
14. M. S. Tamboli, S. A. Patil, A. M. Tamboli, S. S. Patil, N. T. N. Truong, K. Lee, C. S. Praveen, N. K. Shrestha, C. Park and B. B. Kale, *Dalton Trans.*, 2022, **51**, 6027-6035.
15. V. K. V. P. Srirapu, A. Kumar, N. Kumari, P. Srivastava and R. N. Singh, *Int. J. Hydrog. Energy*, 2018, **43**, 16543-16555.
16. M. Rittiruam, N. Aumnongpho, T. Saelee, P. Khajondetchairit, S. Kheawhom, B. Alling, S. Praserthdam, A. Ektarawong and P. Praserthdam, *J. Energy Storage*, 2024, **78**, 110005.
17. P. W. Menezes, C. Walter, J. N. Hausmann, R. Beltrán-Suito, C. Schlesiger, S. Praetz, V. Yu. Verchenko, A. V. Shevelkov and M. Driess, *Angew. Chem. Int. Ed.* , 2019, **58**, 16569-16574.
18. M. Driess, C. Walter, P. Menezes, M. Lerch, S. Orthmann, B. Kaiser, J. Schuch and P. Connor, *Angew.Chem.Int.Ed.*, 2017, **130**, 698-702.
19. P. W. Menezes, C. Walter, B. Chakraborty, J. N. Hausmann, I. Zaharieva, A. Frick, E. von Hauff, H. Dau and M. Driess, *Adv. Mater.*, 2021, **33**, 2004098.
20. C. Walter, S. Kalra, R. Beltrán-Suito, M. Schwarze, P. W. Menezes and M. Driess, *Mater. Today Chem.*, 2022, **24**, 100905.
21. I. Mondal, P. V. Menezes, K. Laun, T. Diemant, M. Al-Shakran, I. Zebger, T. Jacob, M. Driess and P. W. Menezes, *ACS Nano*, 2023, **17**, 14043-14052.
22. H. Sun, S. Chen, B. Zhang, J. Wang, J. Yao, D. Li and G. Yuan, *Dalton Trans.*, 2023, **52**, 17407-17415.
23. R. Srivastava, S. Bhardwaj, A. Kumar, A. N. Robinson, J. Sultana, S. R. Mishra, F. Perez and R. K. Gupta, *Int. J. Hydrog. Energy*, 2024, **49**, 971-983.
24. Y. Zeng, L. Yan, S. Tian and X. Sun, *ACS Appl. Mater. Interfaces*, 2023, **15**, 47103-47110.
25. M. Fekete, R. K. Hocking, S. L. Y. Chang, C. Italiano, A. F. Patti, F. Arena and L. Spiccia, *Energy Environ. Sci.*, 2013, **6**, 2222-2232.
26. Y. Meng, W. Song, H. Huang, Z. Ren, S.-Y. Chen and S. L. Suib, *J. Am. Chem. Soc.*, 2014, **136**, 11452-11464.
27. A. Ramírez, P. Hillebrand, D. Stellmach, M. M. May, P. Bogdanoff and S. Fiechter, *J. Phys. Chem. C*, 2014, **118**, 14073-14081.
28. Y. Zhou, Z. Zhou, L. Hu, R. Tian, Y. Wang, H. Arandiyan, F. Chen, M. Li, T. Wan, Z. Han, Z. Ma, X. Lu, C. Cazorla, T. Wu and D. Chu, *Chem. Eng. J*, 2022, **438**, 135561.
29. Y. Zhao, C. Chang, F. Teng, Y. Zhao, G. Chen, R. Shi, G. I. N. Waterhouse, W. Huang and T. Zhang, *Adv. Energy Mater.*, 2017, **7**, 1700005.
30. A. Gowrisankar and S. Thangavelu, *J. Phys. Chem. C*, 2022, **126**, 3419-3431.
31. W. Sun, Z. Zhou, W. Q. Zaman, L.-m. Cao and J. Yang, *ACS Appl. Mater. Interfaces*, 2017, **9**, 41855-41862.
32. I. G. McKendry, L. J. Mohamad, A. C. Thenuwara, T. Marshall, E. Borguet, D. R. Strongin and M. J. Zdilla, *ACS Energy Lett.*, 2018, **3**, 2280-2285.
33. M.-R. Gao, Y.-F. Xu, J. Jiang, Y.-R. Zheng and S.-H. Yu, *J. Am. Chem. Soc.*, 2012, **134**, 2930-2933.
34. K. Jin, H. Seo, T. Hayashi, M. Balamurugan, D. Jeong, Y. K. Go, J. S. Hong, K. H. Cho, H. Kakizaki, N. Bonnet-Mercier, M. G. Kim, S. H. Kim, R. Nakamura and K. T. Nam, *J. Am. Chem. Soc.* , 2017, **139**, 2277-2285.
35. J. G. Badiger, M. Arunachalam, R. S. Kanase, S. A. Sayed, K.-S. Ahn, J.-S. Ha and S. H. Kang, *Int. J. Hydrog. Energy*, 2024, **51**, 156-168.
36. S. E. Balaghi, C. A. Triana and G. R. Patzke, *ACS Catal.* , 2020, **10**, 2074-2087.
37. H. Singh, M. Marley-Hines, S. Chakravarty and M. Nath, *J. Mater. Chem. A*, 2022, **10**, 6772-6784.
38. J. Guan, Z. Duan, F. Zhang, S. D. Kelly, R. Si, M. Dupuis, Q. Huang, J. Q. Chen, C. Tang and C. Li, *Nat. Catal.* , 2018, **1**, 870-877.
39. F. Cheng, J. Zhao, W. Song, C. Li, H. Ma, J. Chen and P. Shen, *Inorg. Chem.*, 2006, **45**, 2038-2044.